Syed Shoaib Hassan Zaidi

Department of Mechanical Engineering, University of Kansas, Lawrence, KS 66045 e-mail: syed.zaidi@ku.edu

Shusil Sigdel

Department of Physics, Kansas State University, Manhattan, KS 66506 e-mail: ssigdel@ksu.edu

Christopher M. Sorensen

Department of Physics, Kansas State University, Manhattan, KS 66506 e-mail: sor@phys.ksu.edu

Gibum Kwon

Department of Mechanical Engineering, University of Kansas, Lawrence, KS 66045 e-mail: gbkwon@ku.edu

Xianglin Li¹

Department of Mechanical Engineering,
University of Kansas,
Lawrence, KS 66045;
Department of Mechanical Engineering and
Materials Science,
Washington University in St. Louis,
St. Louis, MO 63130
e-mail: xianglinli@ku.edu

Incorporation of Novel Graphene Nanosheet Materials as Cathode Catalysts in Li-O₂ Battery

This study reports the superior performance of graphene nanosheet (GNS) materials over Vulcan XC incorporated as a cathode catalyst in Li– O_2 battery. The GNSs employed were synthesized from a novel, eco-friendly, and cost-effective technique involving chamber detonation of oxygen (O_2) and acetylene (C_2H_2) precursors. Two GNS catalysts i.e., GNS-1 and GNS-2 fabricated with 0.3 and 0.5 O_2/C_2H_2 precursor molar ratios, respectively, were utilized in this study. Specific surface area (SSA) analysis revealed significantly higher SSA and total pore volume for GNS-1 (180 m² g $^{-1}$, 0.505 cm³ g $^{-1}$) as compared with GNS-2 (19 m² g $^{-1}$, 0.041 cm³ g $^{-1}$). GNS-1 exhibited the highest discharge capacity (4.37 Ah g $^{-1}$) and superior cycling stability compared with GNS-2 and Vulcan XC. Moreover, GNS-1 demonstrated promising performance at higher current densities (0.2 and 0.3 mA cm $^{-2}$) and with various organic electrolytes. The superior performance of GNS-1 can be ascribed to its higher mesopore volume, SSA, and optimum wettability compared to its counterparts. [DOI: 10.1115/1.4056937]

Keywords: lithium—oxygen battery, graphene, electrode wettability, current density, Li_2O_2 morphology

1 Introduction

Rechargeable aprotic lithium–oxygen batteries (LOBs) have been considered potential candidates to supersede current rechargeable batteries for next-generation electric vehicles (EV). The Li-ion battery (LIB) is unable to meet the current demands of high energy density in EVs, which are developed to reduce the consumption of fossil fuels. Although LOBs exhibit remarkably high theoretical energy density (11,680 Wh kg $^{-1}$ or \sim 3500 Wh kg $^{-1}$ based on the mass of discharge product, Li₂O₂), the practically achievable energy density is significantly low and estimated between 500 and 900 Wh kg $^{-1}$ [1–6].

The major difference which makes LOB (or metal-air battery) unique from LIB (or metal-ion battery) is the cathodic process. The LIB involves intercalation and deintercalation processes, and the active material is stored within the cathode. On the contrary, the LOB is an open system n which active material (oxygen/air) is supplied from outside through a breathable cathode, which reacts with Li⁺ ions to form Li₂O₂. [7,8]. The possible mechanism is explained in the following electrochemical reaction [9]. During discharging, the reaction begins at the anode where Li metal oxidizes to release Li⁺ ions (Eq. (1)). These Li⁺ ions are transported to the porous cathode through electrolyte where it reacts with incoming O₂/air to form Li₂O₂. This reaction is called oxygen reduction reaction (ORR) as shown in Eq. (2). During charge cycle, the reverse process takes place. The deposited Li₂O₂

decomposes to liberate O_2 and Li^+ ions. This process is called oxygen evolution reaction (OER) as depicted in Eq. (2) [10]. The overall reaction (Eq. (3)) has a theoretical voltage of 2.96 V.

Anode:
$$2Li \leftrightarrow 2Li^+ + 2e^-$$
 (1)

Cathode:
$$2Li^+ + 2e^- + O_2 \leftrightarrow Li_2O_2$$
 (2)

Overall:
$$2\text{Li} + \text{O}_2 \leftrightarrow \text{Li}_2\text{O}_2$$
 (3)

One of the critical challenges that hamper the commercial development of LOB is the design of a porous cathode. The insoluble Li₂O₂ produced during the discharge cycle is stored on the cathode surface. As the discharge cycle continues, Li₂O₂ gradually blocks the transport of electrochemical species to the active sites due to its insulating properties. Consequently, the battery dies out prematurely [11-13]. Therefore, an ideal cathode should have a high surface area (more active sites), high mesopore volume (more storage capacity for Li₂O₂), high porosity (better ion transport), and enhanced stability to withstand the corrosive environment of the battery [14,15]. Due to low cost, high electrical conductivity, and lightness, various carbonaceous materials have been researchers' top priority to incorporate as cathode material [16,17]. It is often decorated with various noble and non-noble metal catalysts, including Pt-Au [18], Pd [19], Pt-Ru [20], RuO₂ [21], α-MnO₂ [22], and Co₃O₄ [23], to improve stability and battery life by reducing charge overpotentials. However, due to the higher surface area of carbon as compared with metal catalysts, the majority of cathode still comprises carbon material (uncovered with catalysts)

¹Corresponding author.

Manuscript received September 30, 2022; final manuscript received January 28, 2023; published online March 7, 2023. Assoc. Editor: Leela Mohana Reddy Arava.

inflicting a critical impact on battery performance. Consequently, it is imperative to search for a cathode material that has properties closest to an ideal cathode for LOB.

Graphene has been employed as a cathode catalyst due to its high electrical conductivity, surface area, and mesopore volume [24]. It has a monolayer, 2D hexagonal lattice structure with sp²-bonded carbon atoms [25]. Bing et al. reported superior performance of graphene in LOB, yielding 2332 mAh g⁻¹ discharge capacity at 50 mA g⁻¹ as compared with Vulcan XC (1645 mAh g⁻¹) [26]. In another study by the same group, they synthesized graphene with various pore sizes and exploited it as a LOB cathode catalyst. The graphene with a bigger pore size (~250 nm) displayed an extremely high discharge capacity of 29,375 mAh g⁻¹ at 200 mA g⁻¹ [27]. Jiuhui et al. doped graphene with N and S before incorporating it as the catalyst and achieved a high discharge capacity (10,400 mAh $\rm g^{-1}$) at 200 mA $\rm g^{-1}$ [28]. Do et al. utilized binder-free graphene nanoplatelets/graphene oxide cathode and obtained a specific discharge capacity of ~6910 mAh g⁻¹ at 200 mA g⁻¹ [29]. Yongliang et al. utilized graphene nanosheets (GNS) as cathode catalysts and achieved a discharge capacity of 8705.9 mAh g⁻¹ at 75 mA g⁻¹. However, they achieved very limited charging capacity (<2,000 mAh g⁻¹) [30].

In this study, we employed graphene nanosheet (GNS) materials with different specific surface areas (SSAs) as LOB cathode catalysts synthesized by a novel, cost-effective, and eco-friendly method involving chamber detonation of oxygen/acetylene mixtures [25,31]. This method yielded graphene in kilograms (1–2) at a low cost. It has been found that SSA of GNS materials can be varied by varying O_2/C_2H_2 (or O/C) precursor molar ratio. SSA of GNSs increases by lowering the O/C molar ratio. The electrochemical performance of LOBs shows that the GNS prepared with the lowest O/C molar ratio (0.3) i.e., GNS-1, outperformed GNS-2 (O/C=0.5) and commercial Vulcan XC owing to its higher mesoporous volume, SSA (as compared with GNS-2) and optimum wettability.

2 Experimental Section

- 2.1 Electrode Preparation. Two graphene materials, GNS-1 (O/C = 0.3) and GNS-2 (O/C = 0.5), were prepared using the detonation technique invented by Dr. Sorensen's group. In a typical detonation, first, we vacuum the chamber to 0.03 atm (absolute pressure). Second, we fill the chamber with the desired molar ratio of the oxygen and acetylene to 1 atm using an electronic flowmeter. Next, the 10 kV spark at the top detonates the mixture. The peak pressure recorded by the piezocrystal at the top of the chamber determines the successful detonation. After a successful detonation, we vent the overpressure gas and open the chamber to collect the carbon sample. Detailed information about the material preparation and characterization can be found in previous publications [25,31]. Vulcan XC 72R and plain carbon cloth (1071 HCB) were purchased from the Fuel Cell Store. For wettability tests, GNS-1 was mixed with polytetrafluoroethylene (PTFE) binder at different weight ratios (C:PTFE = 70:30, 80:20, or 85:15) in isopropyl alcohol (IPA) and water solution (70:30 vol % ratio) to make catalyst mixtures. For all other tests, 30% PTFE content was used. These mixtures were sonicated in a Branson bath sonicator for 3 h to obtain well combined slurry. The resulting slurry was blade coated on plain carbon cloth. The coated substrate was then dried for 24 h at room temperature (20 °C), followed by heat treatment in the oven (SentroTech) at 350 °C for 30 min. The carbon loading for each electrode of area $1.27 \text{ cm}^2 \text{ was } 1.15 \pm 0.2 \text{ mg cm}^{-2}$.
- **2.2 Material Characterization.** The morphology of synthesized GNSs was analyzed under Hitachi SU8230 Regulus ultra-high-resolution Field Emission Scanning Electron Microscope (FESEM) and Hitachi H-8100 High-Resolution Transmission Electron Microscope (HRTEM). Furthermore, the structure of fresh GNSs was analyzed by Raman Spectroscopy and X-ray

Powder Diffraction (XRD) techniques using Invia Reflex Renishaw microspectrometer and D8 ADVANCE diffractometer (Bruker), respectively. SSA measurements were conducted by Nova 1000 series surface area analyzer, and Quantachrome instrument using Brunauer–Emmett–Teller (BET) method. In order to investigate the morphology and elemental composition of the discharge product, deeply discharged graphene cathodes were examined under FESEM and PHI 5000 Versa Probe II X-ray Photoelectron Spectroscopy (XPS), respectively.

- 2.3 Wettability Measurements. To demonstrate the impact of the wettability of GNSs, contact angle (CA) measurements were conducted with GNS-1 (15% and 30% PTFE) and GNS-2 (15% and 30% PTFE) as substrate and 1M DMSO/LiTFSI using a ramé-hart 190-U1 goniometer. Furthermore, electrochemical impedance spectroscopy (EIS) of GNS-1(30% PTFE) and GNS-2 (30% PTFE) was conducted using a Biologic SP-150 potentiostat.
- 2.4 Battery Assembly. Commercially available and widely used organic electrolyte solvents, dimethyl sulfoxide (DMSO), and tetraethylene glycol dimethyl ether (TEGDME) were incorporated in this study. Lithium bis(trifluoromethane)sulfonimide (LiTFSI) was used as Li salt to make 1M concentration solutions. All these materials were purchased from Sigma-Aldrich and used as received. The battery was assembled in an argon-filled Mikrouna glovebox with O2 and H2O concentrations maintained below 0.1 ppm. Figure 1 shows the exploded view of LOB housing utilized in this study. The customized cathode electrode was placed in the customized titanium battery frame, followed by a Whatman glass fiber separator (GF/C, 1822-021) with a diameter of 1.58 cm. Each battery used 90 µL of electrolyte to soak the separator. Finally, a Li chip (0.5 mm thick) with 1.27 cm², acting as the anode, was placed on top of the separator. The battery was screwed appropriately and ready for testing.
- **2.5 Battery Testing.** After taking it out from the glovebox, the battery was connected to a pure O_2 (99.99%) supply. The battery was purged for a minimum of 1 h at the open-circuit voltage (OCV). The charge/discharge capacity experiments were performed on an eight-channel Neware BTS8.0 battery tester. A current density of 0.1 mA cm⁻² was used in all experiments, except for tests using varying current densities. The discharge and charge cutoff voltages used were 2.0 V and 4.5 V, respectively. A number of charge/discharge capacity tests were performed with customized electrodes at room temperature (20 °C).

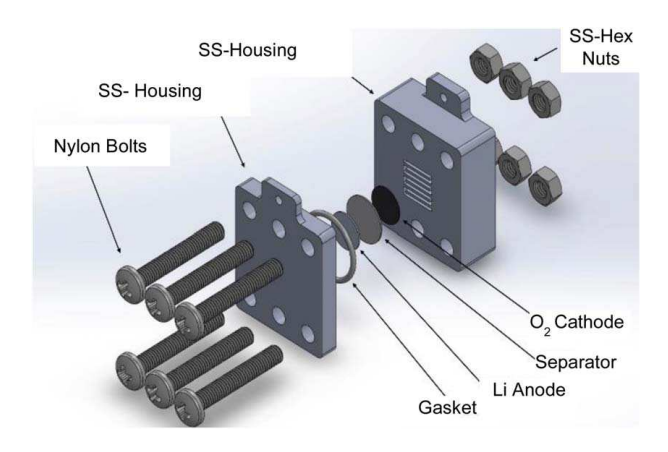


Fig. 1 Exploded view of the serpentine channel housing

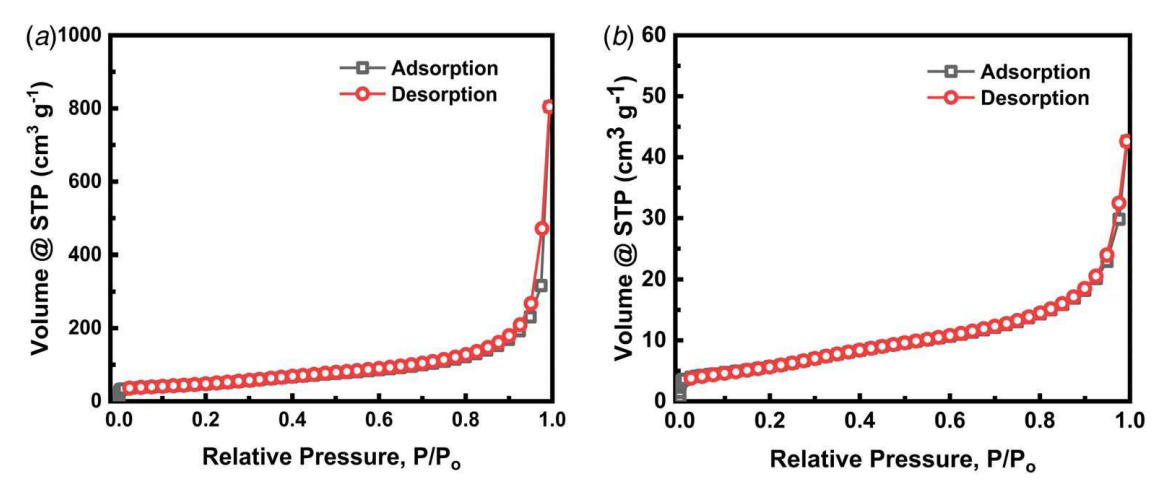


Fig. 2 N2 Adsorption/desorption isotherm of (a) GNS-1 and (b) GNS-2

Table 1 SSA and total pore volume calculated by BET method

Catalyst	Specific surface area (m ² g ⁻¹)	Total pore volume (cm ³ g ⁻¹)
GNS-1	180	0.505
GNS-2	19	0.041
Vulcan XC	233 [30]	0.273 (mesopore volume) [30]

3 Results and Discussion

3.1 Specific Surface Area. SSA and pore volume of cathode materials significantly impact the electrochemical performance of LOB [32]. N₂ adsorption–desorption isotherm measurements were conducted to determine SSAs of graphene materials employed in this study. Figure 2 shows the isotherm plots obtained for GNS-1 (Fig. 2(*a*)) and GNS-2 (Fig. 2(*b*)). Table 1 shows the SSAs and mesopore volume of graphene materials calculated by ET analysis.

GNS-1 exhibits SSA and pore volume of $180~\text{m}^2~\text{g}^{-1}$ and $0.505~\text{cm}^3~\text{g}^{-1}$, respectively. The SSA of GNS-1 is approximately 9.5 times higher than the SSA of GNS-2 ($19~\text{m}^2~\text{g}^{-1}$).

3.2 Material Characterizations of Fresh Samples. Figure 3 shows the SEM and HRTEM images of fresh GNS-1 (left) and GNS-2 (right). SEM images (Fig. 3(a)) of fresh graphene catalysts indicate that with the increasing O/C molar ratio, i.e., from 0. 3 (GNS-1) to 0.5 (GNS-2), the aggregate size also increases. The particle size of GNS-1 is in the range of 50–100 nm. On the other hand, GNS-2 exhibits particle size in the 75–500 nm range. HRTEM images (Fig. 3(b)) show the relatively darker profile of GNS-2 as compared with GNS-1. The darker appearance of GNS-2 agglomerates indicates higher thickness and density due to a higher O/C molar ratio [25]. Furthermore, the structure of graphene materials was examined by Raman spectroscopy (Fig. S1 available in the Supplemental Materials on the ASME Digital Collection) and XRD (Fig. S2 available in the Supplemental Materials) techniques.

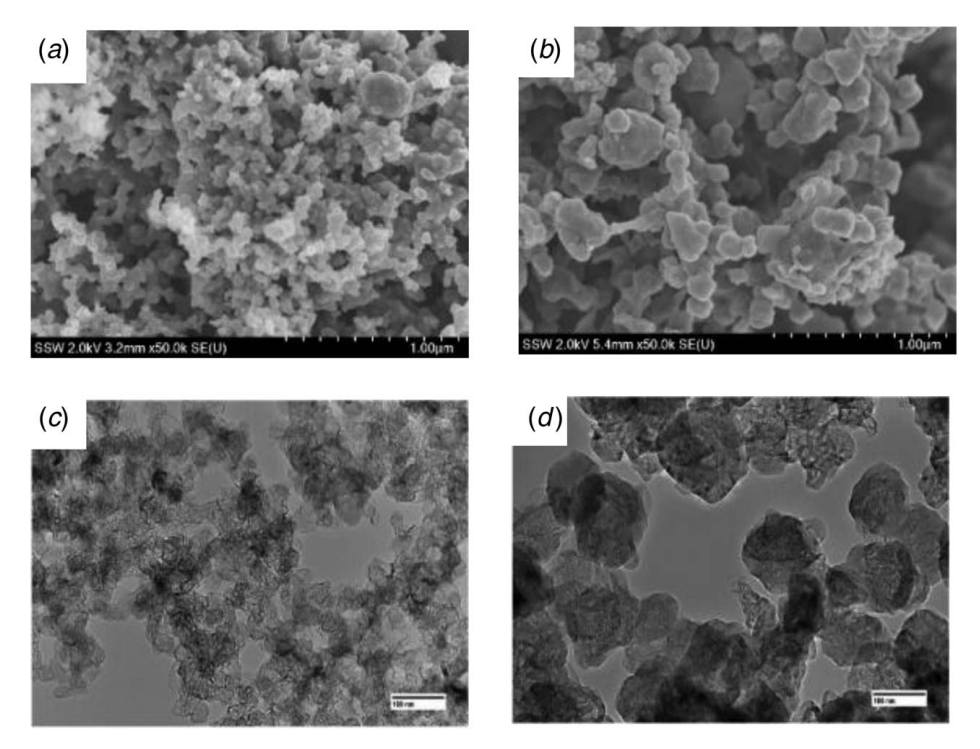


Fig. 3 SEM images of fresh (a) GNS-1 and (b) GNS-2, and HRTEM images of (c) fresh GNS-1 and (d) GNS-2

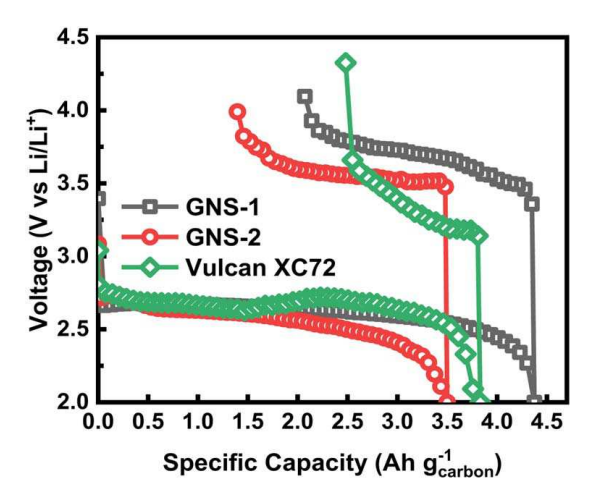


Fig. 4 Comparison of charge/discharge capacity profiles obtained with GNS-1, GNS-2, and Vulcan XC (all with 30% PTFE) using 1M DMSO/LiTFSI at 0.1 mA cm⁻²

The results indicate that the as-prepared GNS-1 and GNS-2 exhibit the characteristic features of graphene materials.

3.3 Deep Discharge Tests. Figure 4 compares the maximum specific charge/discharge capacity cycle obtained with various GNSs and Vulcan XC carbon catalysts. The highest discharge capacity is achieved with GNS-1 (4.37 Ah g $^{-1}$) followed by Vulcan XC (3.83 Ah g $^{-1}$) and GNS-2 (3.50 Ah g $^{-1}$). It is noteworthy that GNS-1 has a lower precursor gas O/C molar

ratio (0.3) than GNS-2 (0.5). The previous study proved [25,31] that increasing the O/C molar ratio during GNS preparation led to a smaller specific surface area (SSA). The maximum SSA was measured for GNS-1 (180 m² g⁻¹) using BET analysis. SSA for GNS-2 decreased substantially as the O/C molar ratio increased. The specific charge/discharge capacity of GNSs incorporated in this study is the depiction of the same trend. The superior performance of GNS-1 over GNS-2 can be attributed to its higher SSA and pore volume. Higher SSA provides more reaction sites for the active species to react, resulting in more discharge product deposition (Li₂O₂). From the literature, the SSA of Vulcan XC lies in the range of 233 m² g⁻¹ but is still outperformed by GNS-1 (with lower SSA). This could be ascribed to different mesopore volumes and pore size distribution (PSD) offered by these materials [30]. A bigger mesopore volume of GNS-1 can provide better access to electrolyte and O₂, effective utilization of electrochemically active

sites, and the accommodation of more discharge products. All these factors lead to higher discharge capacities.

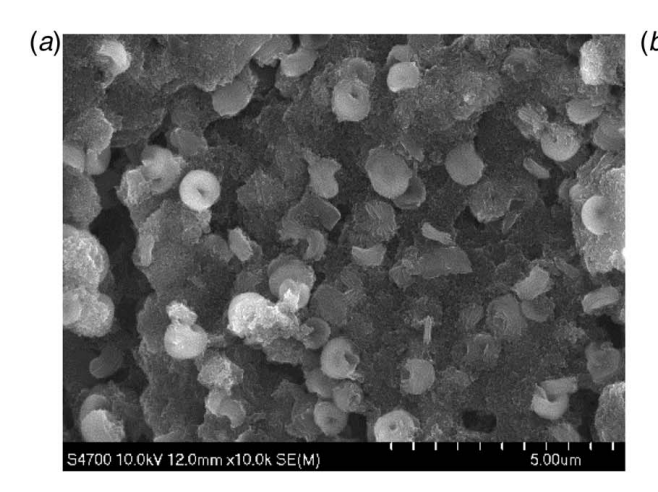
Figure 5 shows the SEM images of (a) GNS-1 and (b) Vulcan XC discharged to the fixed capacity of 1.0 Ah g⁻¹ at 0.1 mA cm⁻² current density. The discharge product Li₂O₂ in the form of big toroids, can be seen distributed among the porous structure of GNS-1 and Vulcan XC electrodes. A closer look at each toroid reveals that they are composed of numerous plate-like structures. This toroidal morphology of the discharge product is consistent with the previous reports in the literature [33,34].

In order to confirm the presence of Li_2O_2 discharge product, we examined the discharged (1.0 Ah g⁻¹) GNS-1 cathode under XPS. Figure 6 shows the XPS spectra, including binding energy curves for Li 1s (Fig. 6(*a*)) and O 1s (Fig. 6(*b*)). The binding energy peaks for Li 1s and O1s appeared at 55.04 eV and 531.6 eV. These values are in good agreement for Li_2O_2 with the previous reports [35,36]. Moreover, the presence of Li_2CO_3 was not detected in the discharged cathode, which typically appears at 55.5 eV in Li 1s spectra [37].

3.4 Cycling Stability. Cycling stability tests were conducted by curtailing the capacity to 1.0 Ah g⁻¹. The cycling stability plots of GNS-1, GNS-2, and Vulcan XC are shown in Fig. 7. GNS-1 yielded five cycles with 1.0 Ah g⁻¹ capacity, followed by GNS-2 with four cycles and Vulcan XC with only three cycles. This indicates enhanced cycling stability of GNS catalysts as compared with Vulcan XC. Superior cycling performance could also be ascribed to better stability and higher mesoporous volume of GNS materials.

It is worth mentioning that cycling stability tests did not yield outstanding results regardless of cathode catalysts. This could be ascribed to Li anode instability and carbon powders' utilization without further treatment with metal catalysts. Nonetheless, GNS materials demonstrated better cycling performance than Vulcan XC.

3.5 Electrode Wettability. Besides SSA, PSD, and mesopore volume of LOB cathode, another factor that significantly impacts the battery's performance while optimizing cathode properties is the wettability. Wettability controls the distribution of electrolytes in the oxygen cathode of LOB [38]. We investigated the effects of wettability on the specific capacity of GNS-1 by varying the carbon-to-binder ratio. In this study, we employed a PTFE binder known for its lyophobic properties. When a cathode surface possesses a higher percentage of PTFE binder, it shows a higher CA of an electrolyte. We measured the CAs of 1M DMSO/LiTFSI on GNS-1 and GNS-2 prepared with varying PTFE binder percentages (15% and 30%) as shown in Fig. 8(a). The results show that a



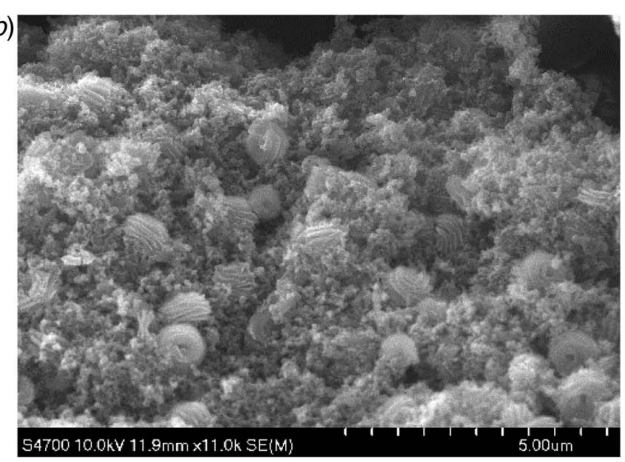


Fig. 5 SEM images of (a) GNS-1 and (b) Vulcan XC discharged to the fixed capacity of 1.0 Ah g⁻¹ at current density 0.1 mA cm

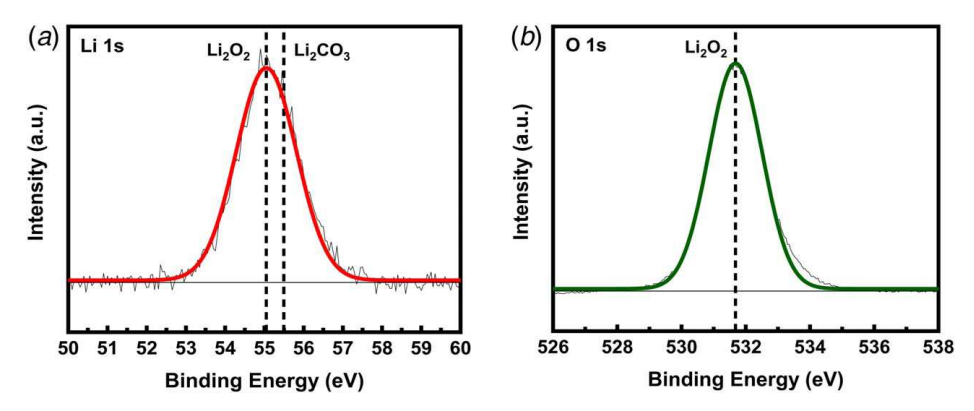


Fig. 6 XPS profile (a) Li 1s and (b) O 1s spectra of discharged GNS-1 cathode to the fixed capacity of 1.0 Ah $\rm g^{-1}$ at current density 0.1 mA cm⁻²

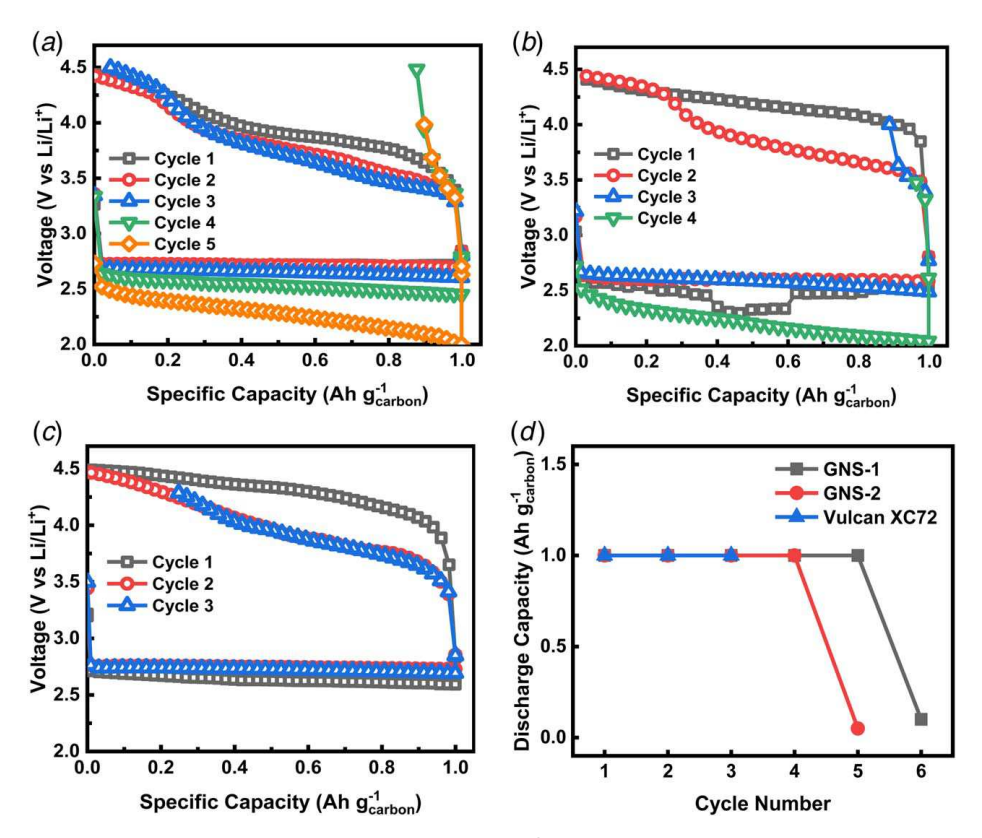


Fig. 7 Cycling stability plots (a)–(c) with 1.0 Ah $\rm g^{-1}$ cutoff capacity using 1M DMSO/LiTFSI at 0.1 mA cm $^{-2}$: (a) GNS-1, (b) GNS-2, (c) Vulcan XC (all with 30% PTFE), and (d) discharge capacity verses cycle number plot

surface with 30% PTFE binder with GNS-1 and GNS-2 exhibits the CA (θ) of 135 \pm 2 deg and 145 \pm 2 deg, respectively, while that with 15% binder shows 98 \pm 2 deg and 115 \pm 2 deg, respectively. These results are intuitive as the CA increases with binder percentage regardless of the graphene catalyst. Previous studies have shown that graphene is hydrophobic in nature [39,40]. It is worth mentioning that GNS-2 displays higher CAs than GNS-1. This could be ascribed to the variation in microstructure and nanostructure caused by different O/C precursor molar ratios. A higher O/C ratio causes more agglomeration of graphene sheets (as shown in SEM and TEM images of fresh samples), which increases the lyophobicity of the material [41]. Since GNS-2 was synthesized with a higher O/C molar ratio, it has shown increased surface lyophobicity than its counterpart GNS-1. The CA results also indicate that the lyophobicity of an electrode can be altered by the type (e.g.,

Nafion, polyvinylidene fluoride (PVDF), and PTFE) and amount of binder incorporated in the fabrication of the electrode.

The EIS measurements were conducted with GNS-1 and GNS-2 with 30% PTFE to study the ohmic resistance offered by each electrode by varying frequency from 100 mHz to 500 kHz. Figure 8(b) shows that GNS-2 exhibits a higher ohmic resistance (bigger x-intercept) at the high-frequency range compared to GNS-1. Similarly, this trend continues to the medium-frequency range, where GNS-2 displays a much larger semicircle which corresponds to higher charge transfer resistance. GNS-1 and GNS-2 show ohmic resistance of 4.62 Ω and 15.04 Ω as calculated by the equivalent circuit model (ECM), shown in Fig. 8(b) inset. This could be attributed to the higher lyophobicity of GNS-2. The wettability presented by GNS-1 is more favorable for LOB application and will be shown later in this section.

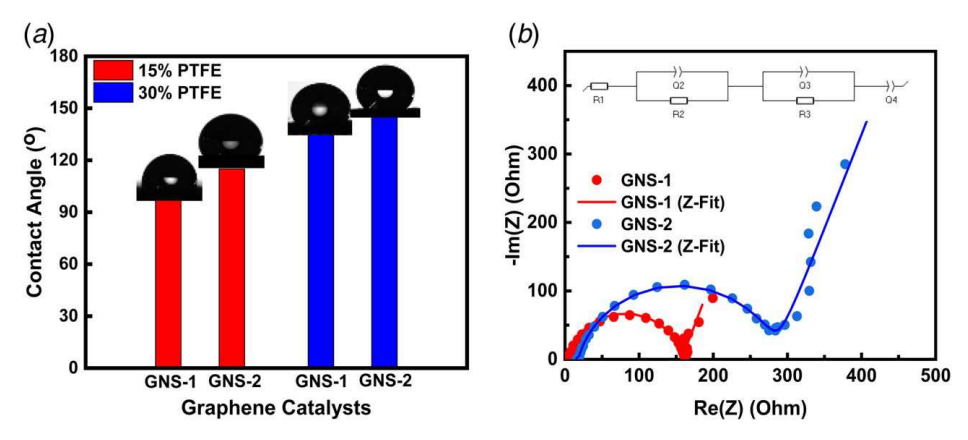


Fig. 8 (a) Contact angle measurements using 1M DMSO/LiTFSI and GNS-1 and GNS-2 with 15% and 30% PTFE substrates. With 15% PTFE, GNS-1 and GNS-2 show 98 \pm 2 deg and 115 \pm 2 deg, respectively, and with 30% PTFE, GNS-1 and GNS-2 show 135 \pm 2 deg and 145 \pm 2 deg, respectively and (b) Impedance spectra of LOB with GNS-1 and GNS-2 with 30% PTFE at open-circuit voltage (OCV); inset: equivalent circuit model

Figure 9 shows charge/discharge capacity profiles obtained with GNS-1 cathodes with various C:PTFE ratios of 85:15, 80:20, and 70:30. GNS-1 yielded 4.37 Ah g⁻¹ with 30% PTFE followed by 3.98 Ah g⁻¹ and 0.41 Ah g⁻¹ with 20% and 15% PTFE content, respectively. GNS catalysts display a clear trend of decline in discharge capacity performance when PTFE content is reduced from 30% to 15%.

The distribution of electrolytes into the porous structure of the oxygen cathode is critical to avoid full saturation of the electrolyte, which slows down oxygen transfer. Instead of a flooded cathode, a partially wetted cathode has been found more efficient for LOB. The cathode with lyophobic properties tends to be partially wetted. It forms a combination of wetted and non-wetted parts deep inside the porous structure. The wetted part includes a thin film of electrolyte on electrochemically active sites of the cathode structure, ensuring the transportation of ions. In contrast, the nonwetted part makes the cathode accessible to oxygen by ameliorating its diffusivity. This approach increases triphase boundaries, which are essential for the reaction. On the contrary, a flooded electrode prevents the faster diffusion of oxygen deep into the cathode surface due to its limited diffusivity and solubility in organic electrolytes. This leads to ineffective utilization of active sites and fewer triphase boundaries. In fact, most of the discharge product

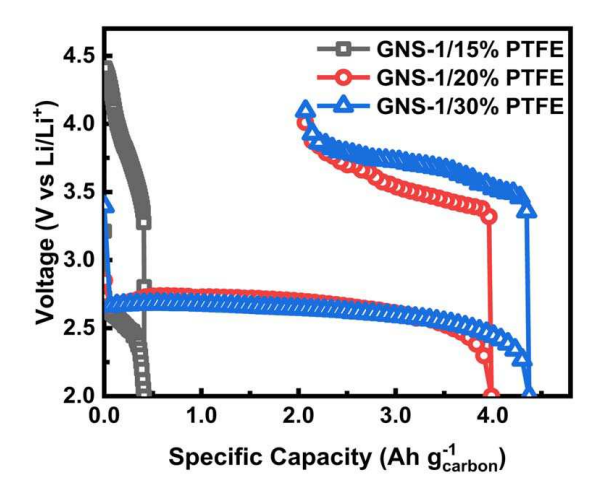


Fig. 9 Comparison of charge/discharge capacity profiles obtained with various GNS-1:PTFE ratios including 85:15, 80:20, and 70:30 using 1M DMSO/LiTFSI at 0.1 mA cm⁻²

accumulates toward the oxygen side of the cathode due to inadequate oxygen diffusivity to the cathode near the separator [42–46].

3.6 Current Density. The low power density has been a bottleneck in the application of LOB. Efforts were made to achieve higher power densities while maintaining a high energy density. The power density of the battery depends on its current density. In this study, GNS-1 and Vulcan XC were subjected to different current densities to investigate their impact on the discharge capacity of LOBs. Figure 10 compares discharge capacity obtained at 0.1, 0.2, and 0.3 mA cm⁻² current densities. A clear trend emerges, which shows discharge capacity decays with increasing current density.

Although Vulcan XC displays a decent discharge capacity at $0.1~\text{mA}~\text{cm}^{-2}$, the discharge capacity quickly fades away at higher current densities. The capacity deterioration can be ascribed to various factors, including sluggish charge transfer, formation of Li_2O_2 layer, and ineffective utilization of active sites of the cathode. The faster electron transfer rate at a higher current density does not allow enough time for the intermediate product, lithium superoxide (Li_2O_2), to undergo solvation in electrolyte and subsequently disproportionation. This leads to the formation of a continuous film of Li_2O_2 by electrochemical reduction on the cathode surface. Due to its insulating nature, it passivates the surface of the cathode, thereby restricting the utilization of active sites available inside the cathode [47,48].

GNS-1 exhibits significantly higher discharge capacity at 0.2 mA cm $^{-2}$ (1.73 Ah g $^{-1}$) and 0.3 mA cm $^{-2}$ (1.43 Ah g $^{-1}$) than Vulcan XC. The superior performance of GNS-1 at higher current densities can be attributed to its higher mesoporous volume, which allows the Li $^{+}$ and O $^{2-}$ to have access to electrochemically active sites for a longer period of time before Li $_2$ O $_2$ passivation layer blocks it completely.

Figure 11 shows the SEM images of the cathode with GNS-1 catalyst discharged to the fixed capacity of 1.0 Ah g $^{-1}$ at the current density of 0.1 mA cm $^{-2}$ (Fig. 11(a)), 0.2 mA cm $^{-2}$ (Fig. 11(b)) and 0.3 mA cm $^{-2}$ (Fig. 11(c)). Figure 11(a) shows that at a lower current density, Li₂O₂ nanocrystals nucleate to form big toroids. On the contrary, at higher current densities, the discharge product accumulated in the form of film, as shown in Figs. 11(b) and 11(c), thereby insulating the cathode surface and premature death of the battery [49,50].

3.7 Electrolyte. The electrochemical performance of LOB incorporated with GNS-1 and Vulcan XC was also investigated with ether-based organic solvent (TEGDME), in addition to DMSO Fig. 12 shows the comparison of specific capacity achieved

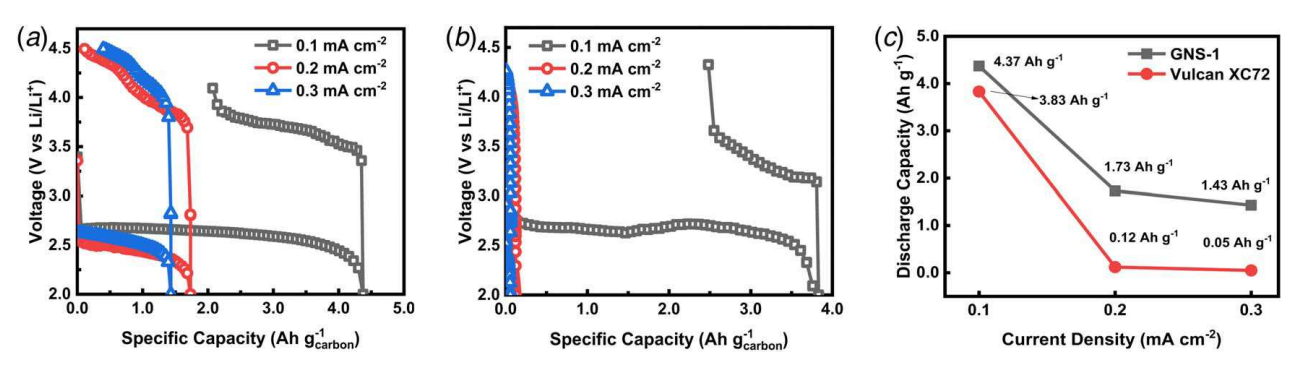


Fig. 10 Comparison of charge/discharge capacity profiles obtained at various current densities including 0.1, 0.2, and 0.3 mA cm⁻² using 1M DMSO/LiTFSI: (a) GNS-1, (b) Vulcan XC (all with 30% PTFE), and (c) discharge capacity versus current density plot

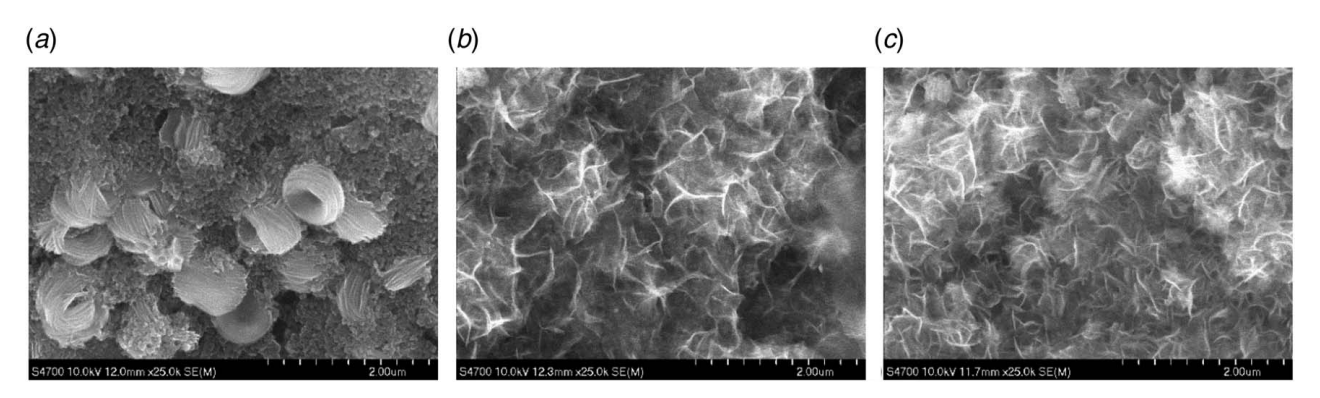


Fig. 11 SEM images of GNS-1 discharged to the fixed capacity of 1.0 Ah g^{-1} at current density: (a) 0.1 mA cm⁻², (b) 0.2 mA cm⁻², and (c) 0.3 mA cm⁻²

with two organic electrolytes. It is evident from Fig. 12 that GNS-1 displays higher discharge capacities with both electrolytes as compared with Vulcan XC. Moreover, regardless of carbon catalysts, the battery employed with DMSO-based electrolyte achieved significantly higher discharge capacity with low potential gap as compared with its counterpart. DMSO-based LOBs yield 4.37 Ah g $^{-1}$ and 3.83 Ah g $^{-1}$, whereas TEGDME-based LOBs exhibit 2.88 Ah g $^{-1}$ and 1.88 Ah g $^{-1}$ with GNS-1 and Vulcan XC, respectively. This could be explained in terms of formation mechanisms of Li₂O₂ and physiochemical properties of respective organic solvents.

Different electrolyte solvents follow different Li₂O₂ formation mechanisms. The way Li₂O₂ accumulates depends mainly on two factors (1) current density and (2) solvent Gutmann donor number (DN). Since the current density is kept consistent at 0.1 mA cm⁻², the DN becomes the limiting factor. During ORR

reaction, the reaction initiates with a one-electron reduction of oxygen to form lithium superoxide (LiO₂), as explained in Eqs. (4a) and (4b). Depending on its solvation in the electrolyte solvent incorporated, it can either undergo a second electron transfer (called electrochemical reduction) and forms Li₂–O₂ film on the surface (Eq. (5)) or dissolves into electrolyte and forms Li₂O₂ by decomposition of LiO₂ (called disproportionation) as shown in Eq. (6) [48,51]. The superior performance of DMSO could be attributed to its higher DN (29.8 kcal mol⁻¹) as compared to TEGDME (16.6 kcal mol⁻¹). Higher DN promotes solution-based Li₂–O₂ deposition i.e., intermediate product LiO₂ dissolves into the electrolyte and is disproportionate to form toroidal Li₂O₂ from the bulk solution to the electrode surface [52]. On the contrary, lower DN supports surface-based Li₂O₂ deposition by electrochemical reduction, which results in the accumulation of thin layers (5–10 nm),

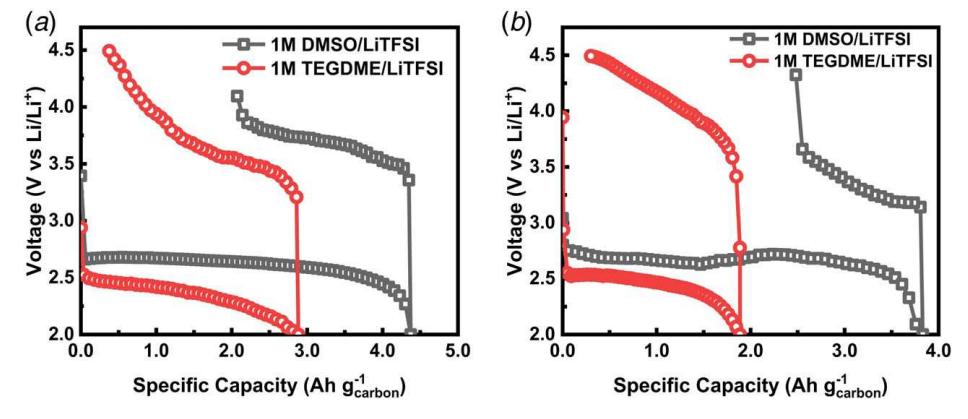


Fig. 12 Comparison of charge/discharge capacity profiles obtained with 1M DMSO/LiTFSI and 1M TEGDME/LiTFSI at 0.1 mA cm⁻²: (a) GNS-1 and (b) Vulcan XC (all with 30% PTFE)

thereby insulating the electrode surface [53]

$$O_2 + e^- \leftrightarrow O_2$$
 (4a)

$$\text{Li}^+ + \text{O}_2^- \leftrightarrow \text{LiO}_2$$
 (4b)

Electrochemical Reduction: $LiO_2 + Li^+ + e^- \leftrightarrow Li_2O_2$ (5)

Disproportionation:
$$2\text{LiO}_2 \leftrightarrow \text{Li}_2\text{O}_2 + \text{O}_2$$
 (6)

This prevents the further mass transfer of reactive species (Li⁺ and O²⁻) from reaching reaction sites resulting in lower discharge capacity. Moreover, DMSO has a higher ionic conductivity (2.11 mS cm⁻¹) and a lower viscosity (1.94 cP) as compared with TEGDME (0.3 mS cm⁻¹ and 4.05 cP) [54–59]. Both these properties have a significant impact on the performance of LOB. Especially, a higher viscosity (η) impedes a faster mass transfer (diffusivity, D), according to Stokes–Einstein equation ($D = kT/(6\pi\eta\alpha)$), which is essential to achieve higher discharge capacity [60].

4 Conclusion

We presented the charge/discharge performance of novel GNSs, produced by chamber detonation of oxygen and acetylene precursors, with various SSAs incorporated as LOB cathodes. Various electrochemical tests including deep discharge, cycling stability, effects of wettability, current density, and electrolyte on the performance of LOB were performed. Among GNS catalysts and Vulcan XC, GNS-1 exhibited superior performance with the highest deep discharge capacity and cycling stability. Moreover, GNS-1 maintained significantly higher discharge capacity even at high current densities than commercial Vulcan XC. The superior performance of GNS-1 can be ascribed to its higher mesoporous volume despite having lower SSA as compared with Vulcan XC. Effects of wettability and electrolyte tests showed that 70:30 carbon-to-binder ratio and 1M DMSO/LiTFSI were optimum for improved performance of LOB, respectively. The novel GNS-1 is inexpensive and available in large quantities.

Acknowledgment

The authors highly appreciate the support from the National Science Foundation (Awards 1833048 and 1941083).

Conflict of Interest

There are no conflicts of interest.

Data Availability Statement

The data sets generated and supporting the findings of this article are obtainable from the corresponding author upon reasonable request.

References

- Wang, F., Li, X., Hao, X., and Tan, J., 2020, "Review and Recent Advances in Mass Transfer in Positive Electrodes of Aprotic Li-O₂ Batteries," ACS Appl. Energy Mater., 3(3), pp. 2258-2270.
- [2] Wang, F., Kahol, P. K., Gupta, R., and Li, X., 2019, "Experimental Studies of Carbon Electrodes With Various Surface Area for Li-O₂ Batteries," ASME J. Electrochem. Energy Convers. Storage, 16(4), p. 041007.
- [3] Zaidi, S.S.H., and Li, X., 2021, "Effects of Oxygen Cathode Substrates with Various Carbon Catalysts on the Discharge Capacity of Lithium-Oxygen Battery," ECS Meeting Abstracts MA2021-01, 350, Chicago, IL, May 30-June 3.
- [4] Zhao, W., Mu, X., He, P., and Zhou, H., 2019, "Advances and Challenges for Aprotic Lithium-Oxygen Batteries Using Redox Mediators," Batter. Supercaps, 2(10), pp. 803–819.
- [5] Hong, Y. S., Zhao, C. Z., Xiao, Y., Xu, R., Xu, J. J., Huang, J. Q., Zhang, Q., Yu, X., and Li, H., 2019, "Safe Lithium-Metal Anodes for Li-O₂ Batteries: From

- Fundamental Chemistry to Advanced Characterization and Effective Protection," Batter. Supercaps, 2(7), pp. 638–658.
- [6] Alvarez-Tirado, M., Castro, L., Guéguen, A., and Mecerreyes, D., 2022, "Iongel Soft Solid Electrolytes Based on [DEME][TFSI] Ionic Liquid for Low Polarization Lithium-O₂ Batteries," Batter. Supercaps, 5(7), p. e202200049.
- [7] Eftekhari, A., and Ramanujam, B., 2017, "In Pursuit of Catalytic Cathodes for Lithium-Oxygen Batteries," J. Mater. Chem. A Mater., 5(17), pp. 7710-7731.
 [8] Xiong, M., and Ivey, D. G., 2019, "Synthesis of Bifunctional Catalysts for
- [8] Xiong, M., and Ivey, D. G., 2019, "Synthesis of Bifunctional Catalysts for Metal-Air Batteries Through Direct Deposition Methods," Batter. Supercaps, 2(4), pp. 326–335.
- 2(4), pp. 326–335.
 [9] Cao, D., Zhang, S., Yu, F., Wu, Y., and Chen, Y., 2019, "Carbon-Free Cathode Materials for Li–O₂ Batteries," Batter. Supercaps, 2(5), pp. 428–439.
- [10] Yilmaz, M. S., Coşkun, M., Şener, T., and Metin, Ö, 2019, "Silica Coated ZnFe₂O₄ Nanoparticles as Cathode Catalysts for Rechargeable Lithium-Air Batteries," Batter. Supercaps, 2(4), pp. 380–386.
- [11] Zhou, W., Zhang, H., Nie, H., Ma, Y., Zhang, Y., and Zhang, H., 2015, "Hierarchical Micron-Sized Mesoporous/Macroporous Graphene With Well-Tuned Surface Oxygen Chemistry for High Capacity and Cycling Stability Li-O₂ Battery," ACS Appl. Mater. Interfaces, 7(5), pp. 3389–3397.
- [12] Hegde, G. S., Ghosh, A., Badam, R., Matsumi, N., and Sundara, R., 2020, "Role of Defects in Low-Cost Perovskite Catalysts Toward ORR and OER in Lithium-Oxygen Batteries," ACS Appl. Energy Mater., 3(2), pp. 1338–1348.
- [13] Huang, J., and Peng, Z., 2019, "Understanding the Reaction Interface in Lithium-Oxygen Batteries," Batter. Supercaps, 2(1), pp. 37–48.
- [14] Nam, J. S., Jung, J. W., Youn, D. Y., Cho, S. H., Cheong, J. Y., Kim, M. S., Song, S. W., Kim, S. J., and Kim, I. D., 2020, "Free-Standing Carbon Nanofibers Protected by a Thin Metallic Iridium Layer for Extended Life-Cycle Li-Oxygen Batteries," ACS Appl. Mater. Interfaces, 12(50), pp. 55756–55765.
- [15] Jung, C. Y., Zhao, T. S., Zeng, L., and Tan, P., 2016, "Vertically Aligned Carbon Nanotube-Ruthenium Dioxide Core-Shell Cathode for Non-Aqueous Lithium-Oxygen Batteries," J. Power Sources, 331, pp. 82–90.
- [16] Bharadwaj, N., Nair, A. S., Das, S., and Pathak, B., 2022, "Size-Dependent Effects in Fullerene-Based Catalysts for Nonaqueous Li-Air Battery Applications," ACS Appl. Energy Mater., 5(3), pp. 3380-3391.
- [17] Greenburg, L. C., Plaza-Rivera, C. O., Kim, J. W., Connell, J. W., and Lin, Y., 2021, "Architecture Transformations of Ultrahigh Areal Capacity Air Cathodes for Lithium-Oxygen Batteries," <u>Batter. Supercaps</u>, 4(1), pp. 120–130.
- [18] Lu, Y. C., Gasteiger, H. A., and Shao-Horn, Y., 2011, "Catalytic Activity Trends of Oxygen Reduction Reaction for Nonaqueous Li-Air Batteries," J. Am. Chem. Soc., 133(47), pp. 19048–19051.
- [19] Lu, J., Lei, Y., Lau, K. C., Luo, X., Du, P., Wen, J., Assary, R. S., et al., 2013, "A Nanostructured Cathode Architecture for Low Charge Overpotential in Lithium-Oxygen Batteries," Nat. Commun., 4(1), p. 2383.
- [20] Zaidi, S.S.H., Rajendran, S., Sekar, A., Elangovan, A., Li, J., and Li, X., 2023, "Binder-Free Li-O₂ Battery Cathodes Using Ni- and PtRu-Coated Vertically Aligned Carbon Nanofibers as Electrocatalysts for Enhanced Stability" Nano Res. Energy.
- [21] Zhou, M., Li, C. Y. V., and Chan, K. Y., 2017, "Advancing Li-O₂ Battery Technology With Durable High Capacity Cathode Composed of Iron-Nitrogen-Doped Mesoporous Core-Shell Carbon Loaded with RuO₂ Nanoparticles," Energy Technol., 5(5), pp. 732–739.
- [22] Qin, Y., Lu, J., Du, P., Chen, Z., Ren, Y., Wu, T., Miller, J. T., Wen, J., Miller, D. J., and Zhang, Z., 2013, "In Situ Fabrication of Porous-Carbon-Supported α-MnO₂ Nanorods at Room Temperature: Application for Rechargeable Li–O₂ Batteries, K. Amine," Energy Environ. Sci., 6(2), pp. 519–531.
- [23] Zhang, P., Wang, Z., Wang, P., Hui, X., Zhao, D., Zhang, Z., and Yin, L., 2022, "Heteroatom Doping-Induced Defected Co3O4 Electrode for High-Performance Lithium Oxygen Battery," ACS Appl. Energy Mater., 5(3), pp. 3359–3368.
- [24] Zhu, L., Scheiba, F., Trouillet, V., Georgian, M., Fu, Q., Sarapulpva, A., Sigel, F., Hua, W., and Ehrenberg, H., 2019, "MnO₂ and Reduced Graphene Oxide as Bifunctional Electrocatalysts for Li–O₂ Batteries," ACS Appl. Energy Mater., 2(10), pp. 7121–7131.
- [25] Wright, J. P., Sigdel, S., Corkill, S., Covarrubias, J., LeBan, L., Nepal, A., Li, J., Divigalpitiya, R., Bossmann, S. H., and Sorensen, C. M., 2022, "Synthesis of Turbostratic Nanoscale Graphene via Chamber Detonation of Oxygen/ Acetylene Mixtures," Nano Select, 3(6), pp. 1054–1068.
- [26] Sun, B., Wang, B., Su, D., Xiao, L., Ahn, H., and Wang, G., 2012, "Graphene Nanosheets as Cathode Catalysts for Lithium-Air Batteries With an Enhanced Electrochemical Performance," Carbon, 50(2), pp. 727–733.
- [27] Sun, B., Huang, X., Chen, S., Munroe, P., and Wang, G., 2014, "Porous Graphene Nanoarchitectures: An Efficient Catalyst for Low Charge-Overpotential, Long Life, and High Capacity Lithium-Oxygen Batteries," Nano Lett, 14(6), pp. 3145–3152.
- [28] Han, J., Guo, X., Ito, Y., Liu, P., Hojo, D., Aida, T., Hirata, A., et al., 2016, "Effect of Chemical Doping on Cathodic Performance of Bicontinuous Nanoporous Graphene for Li-O₂ Batteries," Adv. Energy Mater., 6(3), p. 1501870.
- [29] Kim, D. Y., Kim, M., Kim, D. W., Suk, J., Park, O. O., and Kang, Y., 2015, "Flexible Binder-Free Graphene Paper Cathodes for High-Performance Li-O₂ Batteries," Carbon, 93, pp. 625–635.
- [30] Li, Y., Wang, J., Li, X., Geng, D., Li, R., and Sun, X., 2011, "Superior Energy Capacity of Graphenenanosheets for a Nonaqueous Lithium-Oxygen Battery," Chem. Commun., 47(33), pp. 9438–9440.
- [31] Nepal, A., Singh, G. P., Flanders, B. N., and Sorensen, C. M., 2013, "One-Step Synthesis of Graphene via Catalyst-Free gas-Phase Hydrocarbon Detonation," Nanotechnology, 24(24), p. 245602.

- [32] Xiao, J., Wang, D., Xu, W., Wang, D., Williford, R. E., Liu, J., and Zhang, J.-G., 2010, "Stabilization of Silicon Anode for Li-Ion Batteries," J. Electrochem. Soc., 157(4), p. A487.
- [33] Mitchell, R. R., Gallant, B. M., Shao-Horn, Y., and Thompson, C. V., 2013, "Mechanisms of Morphological Evolution of Li₂O₂ Particles During Electrochemical Growth," J. Phys. Chem. Lett., 4(7), pp. 1060–1064.
- [34] Xia, C., Waletzko, M., Chen, L., Peppler, K., Klar, P. J., and Janek, J., 2014, "Evolution of Li₂O₂ Growth and Its Effect on Kinetics of Li-O₂ Batteries," ACS Appl. Mater. Interfaces, 6(15), pp. 12083–12092.
- [35] Li, J., Han, K., Huang, J., Li, G., Peng, S., Li, N., Wang, J., et al., 2021, "Polarized Nucleation and Efficient Decomposition of Li₂O2 for Ti₂C MXene Cathode Catalyst Under a Mixed Surface Condition in Lithium-Oxygen Batteries," Energy Storage Mater., 35, pp. 669–678.
- [36] Younesi, R., Hahlin, M., Björefors, F., Johansson, P., and Edström, K., 2013, "Li-O₂ Battery Degradation by Lithium Peroxide (Li₂O₂)," Chem. Mater., 25(1), pp. 77–84.
- [37] Kanamura, K., Tamura, H., Shiraishi, S., and Takehara, Z., 1995, "XPS Analysis of Lithium Surfaces Following Immersion in Various Solvents Containing LiBF₄," J. Electrochem. Soc., 142(2), pp. 340–347.
- [38] Kube, A., Bienen, F., Wagner, N., and Friedrich, K. A., 2022, "Wetting Behavior of Aprotic Li–Air Battery Electrolytes," Adv. Mater. Interfaces, 9(4), p. 2101569.
- [39] Jiang, Q. G., Ao, Z. M., Chu, D. W., and Jiang, Q., 2012, "Reversible Transition of Graphene From Hydrophobic to Hydrophilic in the Presence of an Electric Field," J. Phys. Chem. C, 116(36), pp. 19321–19326.
- [40] Xu, Z., Ao, Z., Chu, D., Younis, A., Li, C. M., and Li, S., 2014, "Reversible Hydrophobic to Hydrophilic Transition in Graphene via Water Splitting Induced by UV Irradiation," Sci. Rep., 4(1), p. 6450.
- [41] Zhang, X., Wan, S., Pu, J., Wang, L., and Liu, X., 2011, "Highly Hydrophobic and Adhesive Performance of Graphene Films," J. Mater. Chem., 21(33), pp. 12251–12258.
- [42] Küpper, J., Jakobi, S., and Simon, U., 2021, "PTFE Enhances Discharge Performance of Carbon Cathodes in Potassium-Oxygen Batteries," Batter. Supercaps, 4(10), pp. 1620–1626.
- [43] Zhang, W., Shen, Y., Sun, D., Huang, Z., and Huang, Y., 2017, "Objectively Evaluating the Cathode Performance of Lithium-Oxygen Batteries," Adv. Energy Mater., 7(24), p. 1602938.
- [44] Tan, P., Shyy, W., and Zhao, T., 2015, "What is the Ideal Distribution of Electrolyte Inside Cathode Pores of Non-Aqueous Lithium-Air Batteries?," Sci. Bull., 60(10), pp. 975–976.
- [45] Gao, J., Cai, X., Wang, J., Hou, M., Lai, L., and Zhang, L., 2018, "Recent Progress in Hierarchically Structured O2-Cathodes for Li-O2 Batteries," Chem. Eng. J., 352, pp. 972–995.
- [46] Xia, C., Bender, C. L., Bergner, B., Peppler, K., and Janek, J., 2013, "An Electrolyte Partially-Wetted Cathode Improving Oxygen Diffusion in Cathodes of Non-Aqueous Li–Air Batteries," Electrochem. Commun., 26, pp. 93–96.
- [47] Dutta, A., Ito, K., and Kubo, Y., 2019, "Establishing the Criteria and Strategies to Achieve High Power During Discharge of a Li–Air Battery," J. Mater. Chem. A Mater., 7(40), pp. 23199–23207.

- [48] Liu, C., Sato, K., bin Han, X., and Ye, S., 2019, "Reaction Mechanisms of the Oxygen Reduction and Evolution Reactions in Aprotic Solvents for Li-O₂ Batteries," Curr. Opin. Electrochem., 14, pp. 151-156.
- [49] Adams, B. D., Radtke, C., Black, R., Trudeau, M. L., Zaghib, K., and Nazar, L. F., 2013, "Current Density Dependence of Peroxide Formation in the Li-O₂ Battery and Its Effect on Charge," Energy Environ. Sci., 6(6), pp. 1772–1778.
- [50] Tan, P., Shyy, W., Zhao, T. S., Wei, Z. H., and An, L., 2015, "Discharge Product Morphology Versus Operating Temperature in Non-Aqueous Lithium-Air Batteries," J. Power Sources, 278, pp. 133–140.
 [51] Plunkett, S. T., Wang, H. H., Park, S. H., Lee, Y. J., Cabana, J., Amine, K.,
- [51] Plunkett, S. T., Wang, H. H., Park, S. H., Lee, Y. J., Cabana, J., Amine, K., Al-Hallaj, S., Chaplin, B. P., and Curtiss, L. A., 2020, "Charge Transport Properties of Lithium Superoxide in Li–O2 Batteries," ACS Appl. Energy Mater., 3(12), pp. 12575–12583.
- [52] Augustin, M., Fenske, D., and Parisi, J., 2016, "Study on Electrolyte Stability and Oxygen Reduction Reaction Mechanisms in the Presence of Manganese Oxide Catalysts for Aprotic Lithium-Oxygen Batteries," Energy Technol., 4(12), pp. 1531–1542.
- [53] Yi, X., Liu, X., Dou, R., Wen, Z., and Zhou, W., 2021, "Unraveling the Control Mechanism of Carbon Nanotubes on the Oxygen Reduction Reaction and Product Growth Behavior in Lithium–Air Batteries," ACS Appl. Energy Mater., 4(3), pp. 2148–2157.
- [54] Gittleson, F. S., Jones, R. E., Ward, D. K., and Foster, M. E., 2017, "Oxygen Solubility and Transport in Li–Air Battery Electrolytes: Establishing Criteria and Strategies for Electrolyte Design," Energy Environ. Sci., 10(5), pp. 1167– 1179.
- [55] Laoire, C. O., Mukerjee, S., Abraham, K. M., Plichta, E. J., and Hendrickson, M. A., 2010, "Influence of Nonaqueous Solvents on the Electrochemistry of Oxygen in the Rechargeable Lithium—Air Battery," J. Phys. Chem. C, 114(19), pp. 9178–9186.
- [56] Xu, D., Wang, Z. L., Zhang, L. L., and Zhang, X. B., 2012, "Novel DMSO-Based Electrolyte for High Performance Rechargeable Li-O₂ Batteries," Chem. Commun., 48(55), pp. 6948–6950.
- [57] Korchagin, OV, Bogdanovskaya, V. A., Tripachev, OV, and Emets, V. V., 2018, "Kinetics of Oxygen Reaction and Discharge/Charging Overvoltages of Li-O₂ Battery With Aprotic Electrolytes," Electrochem. Commun., 90, pp. 43–46.
- [58] Rauter, M. T., Augustin, M., Spitthoff, L., and Svensson, A. M., 2021, "Product Formation During Discharge: A Combined Modelling and Experimental Study for Li-O₂ Cathodes in LiTFSI/DMSO and LiTFSI/TEGDME Electrolytes," J. Appl. Electrochem., 51(10), pp. 1437–1447.
- [59] Zaidi, S. S. H., and Li, X., 2021, "Comparing the Electrochemical Performance of Organic and Ionic Liquid-Based Electrolytes in Lithium-Oxygen Battery," ECS Meeting Abstracts MA2021-02, 144, Orlando, FL, Oct. 10–14.
- [60] Read, J., Mutolo, K., Ervin, M., Behl, W., Wolfenstine, J., Driedger, A., and Foster, D., 2003, "Oxygen Transport Properties of Organic Electrolytes and Performance of Lithium/Oxygen Battery," J. Electrochem. Soc., 150(10), p. A1351.